

## EFFECTS OF SCANNING SCHEMES ON LASER TUBE BENDING

Jie Zhang<sup>1</sup>, Peng Cheng<sup>1</sup>, Wenwu Zhang<sup>2</sup>, Michael Graham<sup>2</sup>,  
Jerry Jones<sup>3</sup>, Marshall Jones<sup>2</sup>, Y. Lawrence Yao<sup>1</sup>

<sup>1</sup>Department of Mechanical Engineering, Columbia University, New York, NY

<sup>2</sup>Global Research Center, General Electric Co., Niskayuna, NY

<sup>3</sup>Native American Technologies, Co., Golden, CO

### Abstract

Four laser scanning schemes for tube bending, including point-source circumferential scanning, pulsed line-source axial procession, line-source axial scanning without and with water cooling are investigated in numerical simulation. The coupled thermo-mechanical model established using the finite element method is validated and applied to predict the bending deformation and help better understand bending mechanisms under different schemes. The influence of important parameters such as beam coverage, scanning velocity and cooling offset on the deformation is investigated in detail. Parametric studies are carried out to determine proper processing windows at which the largest bending can be obtained. The deformation characteristics, including the wall thickness variation and the cross-section distortion produced by different scanning schemes are analysed, along with the processing efficiency.

### Introduction

Tube bending has many applications including the automotive and aerospace industries. So far, mechanical bending has been the major technique used in the industry. Mechanical tube bending has the limitation of the minimal bending radius due to material thinning at the extrados. Pressure bending may be adopted to reduce material thinning at extrados. At the intrados, compressive stress may induce the buckling and wrinkling of the material. Mandrels can be used to prevent these forming defects. However, both of pressure bending and mandrels increase the complexity of mechanical bending facilities. In addition, mechanical tube-bending requires complex tooling for multi-axis bending. Hydro-forming of tubular components has attracted significant interest in recent years but it requires hard tooling. As a spring-back-free and die-less technique, laser forming accomplishes the forming task by intensively and locally heating the workpiece and thus inducing thermal deformation. In laser tube-bending, material thinning at the extrados is nearly absent. With

the flexible delivery of laser beam, multi-axis tube bending can be readily realized.

Laser tube bending is normally done via scanning a point laser source along tube circumference, as shown in Fig. 1a. Silve, et al [1] investigated the effects of different scanning sequences on bent tube profile. Kraus [2] analysed the temporal development of plastic straining and restraining in the laser bending of square cross-section tubes with Finite Element Analysis. It was found that plastic restrain primarily occurs in the cooling-off phase. Li and Yao [3] studied the laser bending mechanism of circular cross-section tubes of mild steel. The deformation characteristics such as wall thickness variation, ovality, and protruded intrados were compared with those of mechanical bending. But the circumferential scanning scheme with a point laser source achieves a very small bending angle per scan, and thus requires multiple scans at the same location or at different axial positions in order to obtain practical bending angles.

The advent of high power direct diode lasers offers a rectangular laser beam shape, among other advantages. The rectangular beam shape is well suited for surface processing. Bachmann [4] described how direct diode lasers were applied into surface hardening, cladding and soldering. The application of direct diode lasers into laser forming of plates has also been investigated. Lawrence [5] conducted a comparative investigation of the efficiency of CO<sub>2</sub> laser and diode laser in the forming of mild steel sheets. Lopez, et al. [6] applied a diode laser in the forming of stainless steel, AlMg3 and St 14 sheets and investigated the correlation between bending angle and parameters such as path feed rate, number of irradiations, sheet materials and sheet thickness.

The technique of beam shaping can also transform a circular beam into non-circular shapes. Shealy [7] presented an overview of the development and applications of the various geometrical methods for laser beam shaping. The influence of different beam shape on the processing results has been studied by

several scientists. Mucha, et al. [8] studied the effects of circular and rectangular beam on the deformation of plates. Triantafyllidis, et al. [9] studied the effect of various beam shapes on cooling rate in laser surface treatment of ceramics.

The availability of laser beam with a rectangular shape opens up the possibility of axial scanning in laser tube bending. By eliminating the need for many circumferential scanning passes, which is time consuming, an axial scanning of a rectangular (or line) source can potentially generate sufficient bending in a single axial scanning. It is important to understand the process. It is the aim of this paper to numerically study the bending mechanism, bending characteristics, and suitable operation conditions of various schemes of axial scanning by a line source in comparison with circumferential scanning by a circular (or point) source.

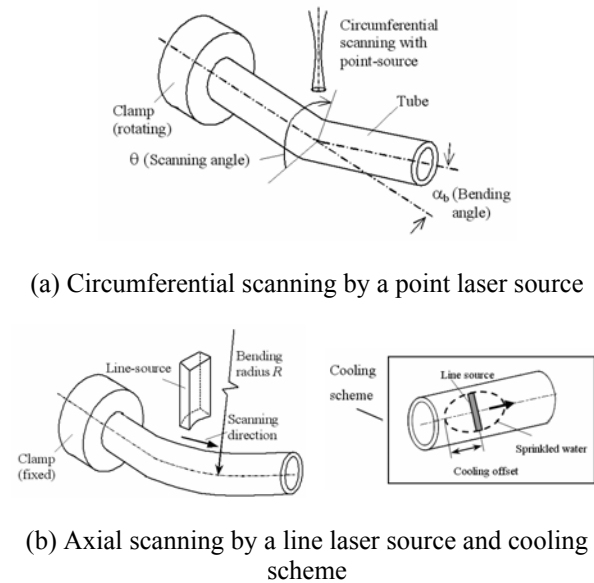


Fig. 1 Schematic of scanning schemes

### Scanning Schemes

Continuous point-source circumferential scanning (referred as Scheme I) refers to a circular beam irradiating along the tube circumferential direction, as shown in Fig. 1a. Multiple scans at the same or different axial positions are normally required to generate sufficient bending. In this paper, the inclusion of Scheme I is for the purpose of validating the numerical model established in the present paper with existing experimental results, and comparatively studying it with different axial scanning schemes. More details about this scanning scheme can be found in [3].

Scanning Scheme II involves a pulsed line-source procession along tube axis. Inclusion of this scheme is primarily for gaining preliminary understanding of axial scanning and thus leads to the following two scanning schemes. Continuous line-source axial scanning is shown in Fig. 1b and is referred to as Scanning Scheme III. It is expected that bending efficiency will be enhanced under this Scheme. Continuous line-source axial scanning with water cooling, referred to as Scheme IV, is also investigated. Under Scheme III, the axial mechanical constraint exerted by unheated materials on the currently heated material is somewhat reduced by scanning-caused heat accumulation. This situation will be worse in the case of long tubes which are particularly suitable for line-source axial scanning. Therefore, it is necessary to remove the amassed heat at the appropriate time. The four scanning schemes are summarized in Table 1.

Table 1 Four Tube Scanning Schemes

No.	Scheme	Beam Shape	Scanning Direction
I	Continuous point-source circumferential scanning	Circular	Circumferential
II	Pulsed line-source axial procession	Rectangular	Axial procession
III	Continuous line-source axial scanning	Rectangular	Axial
IV	Continuous line-source axial scanning with water cooling	Rectangular	Axial

### Laser Sources and Tube Parameters

In the simulation of point-source scanning, the laser system is considered to be CO<sub>2</sub> laser with a maximum output power of 1500W. The power density follows a Gaussian distribution. In the simulation of line-source scanning, the laser system is considered to be diode lasers with a maximum output power of 4000W. The high power diode laser has a rectangular beam shape with 1 to 6 mm in width and 3 to 20 mm in length. The energy intensity is Gaussian distribution in the width direction and top-hat in the length direction. Under all Schemes, it is supposed that the tube is coated with graphite to enhance the absorption of laser power. The material of tube is low carbon steel, AISI1010. The outside diameter of tube is 12.7mm, the thickness of tube is 0.89mm, and the tube length is 100mm. Under Scheme II and III, tube with the length of 50 mm is also modelled to reduce computational time of FEM. Tube length of 600mm is also simulated to validate the feasibility of Scheme IV in the long

tube bending. The simulated processing conditions are listed in Table 2.

Table 2 Processing Conditions\*

Scheme	Power (W)	Velocity (mm/s)	Beam size (mm)	Beam coverage
I	780	1.57 (rad/s)	d=11	180 <sup>0</sup> (scanning angle)
II	200-800	1-6	w=1-6	30 <sup>0</sup> -180 <sup>0</sup>
III	200-600 1350-2000	4-50	w=4	120 <sup>0</sup>
IV	425 and 1550	4 and 20	w=4	120 <sup>0</sup>

\*d is the diameter of circular beam; w is the width of rectangular beam

### Cooling Arrangement

Due to its higher heat-transfer coefficient, water cooling is applied in axial scanning instead of air cooling. An elliptical water sprinkler is assumed to be coaxial with laser beam to move with the laser in synchronization, as shown in Fig. 1b. Water is sprinkled only along the elliptical edge of the sprinkler and other parts of the sprinkler are sealed. The major axis of the sprinkler is coincident with the tube axis and its length can be adjusted to suit different scanning speeds. The minor axis has the same length as the rectangular beam length. The half length of the major axis of the sprinkler is defined as *cooling offset*. The reason that the sprinkler was designed to be elliptical is that the mechanical constraint can be enhanced in the circumferential direction and adjusted in the axial direction.

It is assumed that water flows out of the sprinkler under gravity and covers the entire tube surface except the elliptical area where laser irradiates. The heat-transfer coefficient of water on tube can be evaluated with the model of tube in the cross-flow [10]. The Nusselt number is calculated as

$$N_{ud} = 0.3 + \frac{0.62R_e^{1/2}P_r^{1/3}}{\left[1 + (0.4/P_r)^{1/4}\right]^{1/4}} \left[1 + \left(\frac{R_e}{282,000}\right)^{5/8}\right]^{4/5} \quad (1)$$

which is valid for the range of  $10^2 < R_e < 10^7$  and  $P_{ed} > 0.2$ . Thus, the heat-transfer coefficient is defined by

$$h = N_{ud} \left(\frac{k}{D}\right) \quad (2)$$

where  $k$  is the thermal conductivity and  $D$  is the outer

diameter of tube.

### Numerical Simulation

The following assumptions have been made in the numerical simulation. The tube material is isotropic, and has constant density. Material properties such as the modulus of elasticity, heat transfer properties, thermal conductivity, specific heat and flow stress are temperature dependent and the flow stress is also strain and strain rate dependent. Heat generated by plastic deformation is negligible compared with intensive heat input from the laser beam. No melting and no external forces are involved in laser bending.

Laser tube bending is numerically simulated as a sequentially-coupled thermal-mechanical process. In the thermal analysis, the temperature distribution of the tube can be described by

$$\rho c_p \frac{\partial T}{\partial t} = \nabla(k\nabla T) \quad (3)$$

where  $\rho$  is the density,  $c_p$  the specific heat. The associated boundary condition of the heat conduction equation is  $AF_l \cdot \hat{n} = -\hat{n} \cdot (k\nabla T)$  at  $r=D/2$ , where  $A$  is the absorption coefficient of material,  $F_l$  is the heat flux of laser beam, and  $\hat{n}$  is the unit vector normal to the surface pointing to the tube. All the surfaces are subject to heat convection  $q = h(T - T_0)$ , where  $h$  is the convective heat-transfer coefficient,  $T$  is the surface temperature and  $T_0$  is the ambient temperature. The heat radiation is  $q = \varepsilon\sigma(T^4 - T_0^4)$ , where  $\varepsilon$  and  $\sigma$  are emissivity and Stephan-Boltzmann constant, respectively.

Without the consideration of body forces, the following equation of equilibrium is satisfied due to no external forces exerting on the tube,

$$\frac{\partial \sigma_{ij}}{\partial x_j} = 0 \quad (4)$$

The mean strain rate is written as  $\dot{\varepsilon}_{kk} = \frac{1-2\nu}{3E} \dot{\sigma}_{kk} + \alpha \dot{T}$ ,

where  $E$  is Young's modulus,  $\nu$  is Poisson's ratio,  $\dot{\sigma}_{kk}$  is the mean stress and  $\alpha$  is the thermal expansion coefficient. The deviatoric strain  $e_{ij}$  including elastic strain  $e_{ij}^e$ , viscoelastic strain  $e_{ij}^v$  and plastic strain  $e_{ij}^p$  is written as

$$\dot{e}_{ij} = \dot{e}_{ij}^e + \dot{e}_{ij}^v + \dot{e}_{ij}^p \quad (5)$$

where  $\dot{\epsilon}_{ij}^e = \frac{1}{2G}\dot{s}_{ij}$ , and  $\dot{\epsilon}_{ij}^v = \frac{1}{2\eta}\dot{s}_{ij}$ . Where  $G$  is the shear modulus,  $\eta$  the viscosity constant and  $s_{ij}$  the principal component of the deviatoric stress tensor. When Von Mises criterion  $\sqrt{\frac{3}{2}(\sigma'_{ij}\sigma'_{ij})} = Y$  is used as the yield criterion, the plastic strain follows the flow rule, that is

$$e_{ij}^p = 0 \quad \text{if } \frac{1}{2}s_{ij} \leq Y^2(T), \text{ or if } \frac{1}{2}s_{ij} = Y^2(T) \quad (6)$$

$$\text{and } s_{ij}\dot{s}_{ij} - 2YY\dot{T} \leq 0$$

$$e_{ij}^p = \dot{\lambda}s_{ij} \quad \text{if } \frac{1}{2}s_{ij} = Y^2(T) \quad (7)$$

$$\text{and } s_{ij}\dot{s}_{ij} - 2YY\dot{T} \geq 0$$

where  $\dot{s}_{ij}^v = 2G(\dot{\epsilon}_{ij} - \dot{\epsilon}_{ij}^v)$ , and  $Y(T)$  is the Von Mises yield stress as a function of temperature. Therefore, the combined stress-strain relations can be expressed as

$$\dot{\epsilon}_{ij} = s_{ij}\dot{\lambda} + \frac{1}{2G}\dot{s}_{ij} + \delta_{ij}\left(\frac{1-2\nu}{3E}\right)\dot{\sigma} + \delta_{ij}\alpha\dot{T} \quad (8)$$

Due to the characteristics of laser tube bending, nonlinear analysis is used in the model of finite element analysis (FEA). A commercial FEA software *ABAQUS* is used. The same mesh is created for both heat transfer and structural analysis. In structural analysis, element of C3D20 without shear locking and hourglass effect, is suitable for a bending-deformation-dominated process such as laser forming. To remain compatible with the structural analysis, three-dimensional heat transfer elements of DC3D20 are used for the heat transfer analysis. A user-defined subroutine is developed in FORTRAN to describe the heat flux from the laser beam. All the points in the plane at  $z=0$  are removed of the freedom in the axial direction. Two adjacent points at the bottom of the plane at  $z=0$  are fixed to eliminate the rigid body motion.

## Results and Discussions

### Continuous Point-Source Circumferential Scanning

To validate the FEM model of tube bending established in the present paper, Scheme I is first considered. Fig. 2 shows the comparison of bending angle simulated in the present paper and the existing experimental results of [3]. It is seen that the simulated results agree with the experimental results. Therefore, the numerical model is capable of simulating laser tube bending.

Under Scheme I, the temperature gradient in the tube thickness direction within the heat affected zone is small due to the large beam size used. The condition induces upsetting and subsequent bending. Another known phenomenon is a protrusion at the intrados under Scheme I [3]. Intrados is defined as the inside arc of the bent tube, and extrados is the outside arc of the bent tube. Figure 3 shows the distribution of axial plastic strain along the circumferential direction at the location slightly off the centre of heat affected zone produced by one scan pass. It is seen that the axial plastic strain at the outer surface is larger than that at the inner surface, while the trend reverses at the centre of heat affected zone. This causes the protrusion in the intrados. Note that it is more convenient to use axial plastic strain at this location to analyse the bending process because it is more in line with existing understanding of the process while that at centre location provides confounded information.

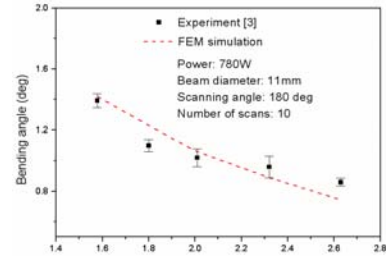


Fig. 2. FEM simulation validation with experimental results (Scheme I)

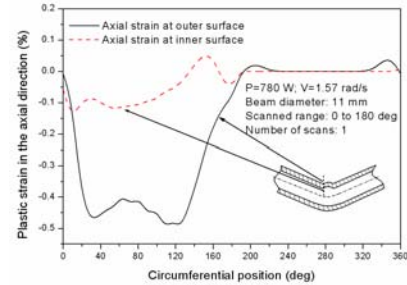


Fig. 3 Distribution of axial plastic strain along the circumferential position at the location slightly off the centre of heat affected zone under Scheme I

### Pulsed Line-source Axial Procession

#### Mechanism of Pulsed Line-source Axial Procession

Under Scheme II, the tube is irradiated in an axial procession of a pulsed line source, which is simplified as a series of stationary pulses sequentially applied at different axial locations. Fig. 4 shows the cur-off schematic of tube bent by one of these pulses at a particular location to investigate the net deformation induced by one pulse to better understand this scanning

scheme. The pulsed beam is 4 mm in width and is assumed to radially irradiate part of tube surface (120 degrees). Given the tube diameter of 12.7mm, the beam is 13.3mm in length. As a result, a strip of material with the same size as the beam is heated simultaneously. Comparing with the tube thickness, the beam size is large. Fig. 4 also shows a distribution of the axial plastic strain along the intrados similar to that under Scheme I (Fig. 3). One protrusion at the intrados can be seen in Fig. 4. It is clear that the pulsed line-source axial procession under the processing condition used bends tube through the upsetting mechanism.

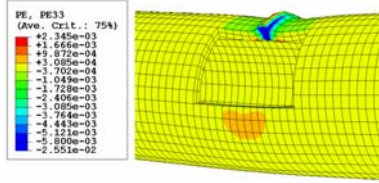


Fig. 4 Cut-off schematic of bent tube with axial plastic strain distribution under Scheme II (deformation  $\times 50$ , irradiating time: 1 sec, beam width: 4mm, energy intensity:  $8\text{J/mm}^2$ )

Effect of Beam Coverage The laser-irradiated range along the tube circumference is referred to as *beam coverage*. In [3], it was found that  $270^\circ$  was properly the optimal scanning angle (equivalent to beam coverage here) under Scheme I. Under the pulsed line-source axial procession scheme, beam coverage perhaps influences the tube bending more significantly because bending through the simultaneous heating of a strip of tube material makes more important the mechanical constraint in the circumferential direction, which likely depends on the beam coverage. Due to the geometrical characteristics of a line source, the beam coverage is restricted to the range below  $180^\circ$ .

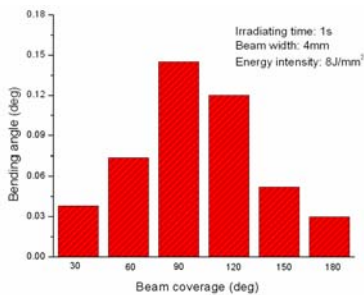


Fig. 5 Relationship of beam coverage with bending angle under Scheme II

Fig. 5 shows the change of bending angle with the beam coverage under the same laser intensity. It is seen that the bending deformation increases with the beam

coverage to a maximum value, before it drops. In order to eliminate the effect of energy intensity, the laser power is adjusted to keep the constant energy intensity of  $8\text{J/mm}^2$  for different beam coverage values. Thus, material almost experiences an identical thermal cycle to thermally expand to the same extent with different beam coverage. The variation of bending angle with the beam coverage comes from the difference in the mechanical constraint.

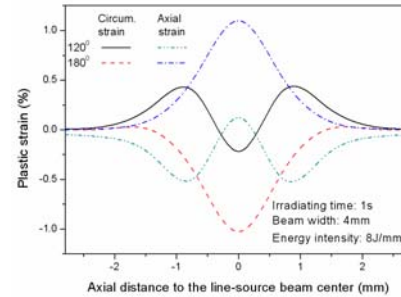


Fig. 6 Distribution of the circumferential- and axial-plastic strain at outer surface along the intrados under Scheme II

Fig. 6 presents the distribution of axial and circumferential plastic strain at the outer surface along the intrados with the beam coverage of  $120^\circ$  and  $180^\circ$ . It can be seen that at each location the magnitudes of plastic strain in axial and circumferential directions are almost the same while the direction (tensile or compressive) are opposite, so that the variation of tube thickness can be neglected if assuming the volume constancy. In the case of  $180^\circ$ , the axial plastic strain remains tensile and the circumferential plastic strain remains compressive. This is because that the mechanical constraint in the axial direction decreases as a result of simultaneous  $180^\circ$  circumferential heating. The tensile strain in the axial direction causes the circumferential strain to be compressive in order to maintain volume constancy. As a result, the bending angle almost diminishes under  $180^\circ$  beam coverage because a compressive axial strain is primarily responsible for bending. In the case of  $120^\circ$  beam coverage, it is better to examine a location slightly off the beam center because of the reason stated early under Scheme I. It is seen that the axial plastic strain is compressive and the circumferential strain is tensile. This is because the  $120^\circ$  beam coverage better preserves the mechanical constraint in the axial direction and thus a larger bending angle is resulted.

To illustrate the point more closely, Fig. 7 shows the time history of axial and circumferential plastic strain at the outer surface slightly off the beam center. For the case of  $120^\circ$  beam coverage, the axial strain is momentarily tensile before it quickly becomes deeply

compressive due to the larger restriction from the surrounding material. As a result, a much larger bending angle is obtained.

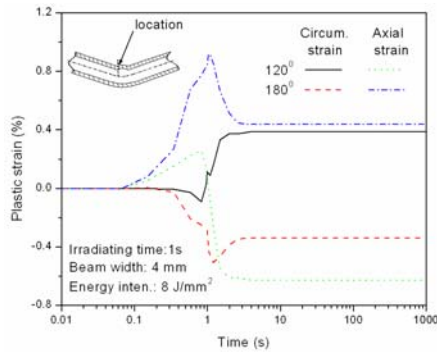


Fig. 7 Time history of circumferential- and axial-plastic strain of outer surface at the location slightly off the line-source center under Scheme II

**Parametrical Study Design of Experiment (DOE) [11]** is applied in the search of better processing parameters for Scheme II. Considering the processing parameters of the circumferential scanning, the limits of available diode lasers, and the requirement of no melting, the initial value of the DOE is set for laser power ( $x_1$ ) as 300W and 700W, irradiating time ( $x_2$ ) as 0.5sec and 1.5sec, and beam width ( $x_3$ ) as 3mm and 6mm. The beam coverage is set as constant of  $120^\circ$ . The DOE experiments are carried out via FEM simulation. The response is bending angle and is described by a first-order model  $\hat{y} = b_0 + bx^T$ , where  $\hat{y}$  and  $x = [x_1, x_2, x_3]^T$  are estimated response and decision variable vector, respectively,  $b = [b_0, b_1, b_2, b_3]^T$  are coefficients determined using the least square regression. A series of responses in the steepest ascent direction are calculated and compared with the corresponding simulation results to adjust the steepest ascent direction. Through five adjustments, the final first-order model is obtained as  $\hat{y} = 0.166 + 0.421x_1 + 0.306x_2 - 0.085x_3$ . This model reflects that the bending angle increases linearly with laser power and irradiating time, and decrease linearly with the beam width. For the tube with the specification mentioned before, the optimal processing parameters are determined as laser power of 425 W, irradiating time of 1 second and beam width of 4mm under this pulsed line-source axial procession scheme.

### Continuous Line-source Axial Scanning

**Mechanism of Continuous Line-source Axial Scanning** Continuous line-source axial scanning (Scheme III) can be viewed as a series of rectangular pulses packed very closely irradiating a tube successively at a high frequency. As the moving beam reaches a particular

location, the heated material there tends to expand thermally. Although the mechanical constraint from the material preceding this location decreases to some extent due to preheating, the materials in other directions can still confine the heated material from freely expanding. As a result, compressive plastic strain occurs in the heated material and tube bends. Fig. 8 shows a bent tube scanned under Scheme III and it also shows axial plastic strain distribution, which is mostly compressive at the outer surface and inner surface. Clearly, Scheme III is still dominated by the upsetting mechanism. In continuous line-source axial scanning, the bending of tube is better described by bending radius instead of bending angle, assuming the radius is largely constant for a particular bend. Unlike bending angle, the bending radius does not depend on tube length.

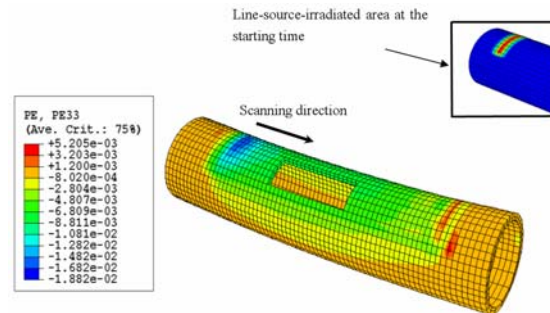


Fig. 8 FEM contour of axial plastic strain under Scheme III (deformation  $\times 5$ , laser power: 1550W, scanning velocity: 20mm/s, beam width: 4mm)

**Parametric Study** The processing parameters under Scheme III are investigated. The optimal processing parameters in Scheme II may not be applicable here since a continuous moving heating source is involved. It is clear that the scanning velocity plays a key role in the deformation of tube under this Scheme. Thus, a constant peak temperature approach [12] is used to specify power and velocity levels that produce about the same peak temperature. Fig. 9 shows the variation of bending radius with these velocity levels. It can be seen that the bending increases first then decreases when the scanning velocity increases, and the minimum bending radius is generated at the velocity around 20mm/s. Two cases are selected for analysis.

A typical temperature distribution along the tube intrados at the time when the beam centre reaches the same point at two different velocities is shown in Fig. 10. At the high velocity of 20mm/s, the heat dissipation is smaller than that at the low velocity so that the temperature difference between scanned material and cold material is steeper. Therefore, the cold material can apply larger constraint on the heat

affected zone which helps to increase the compressive strain. Moreover, more material at high temperature is also helpful to the increase of final deformation. At low velocity of 4mm/s, the temperature tends to increase evenly in the scanned area, which is disadvantageous for cold material to restrict the thermal expansion. The distribution of axial plastic strain along the intrados at two different velocity values is plotted in Fig. 11. The pattern that the axial plastic strain under higher speed (20 mm/s) is larger than that under lower speed (4 mm/s) with the almost identical peak temperature on the scanned surface observed in Figure 10 is in good agreement with the above analysis.

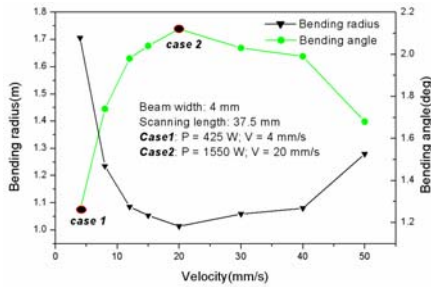


Fig. 9 Variation of bending angle with velocity under a constant peak temperature approach under Scheme III

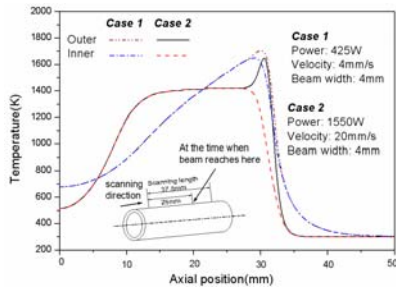


Fig. 10 Comparison of temperature distribution along the intrados at one specific time under Scheme III

It is also shown in Fig.10 that the temperature gradient between the outer and inner surfaces increases with the velocity. Within a certain range of velocity values, the different strain between the outer and inner surfaces due to the temperature difference is not large enough to change the mechanism of tube bending. However, if velocity continues increasing, the Temperature Gradient Mechanism becomes more dominant in the deformation of the upper half tube. Only the outer surface has a large strain, and the inner surface with a small or no strain turns to help the cold lower half tube to impede the tube to bend toward the laser beam. As a result, the bending deformation reduces and the bending radius goes up.

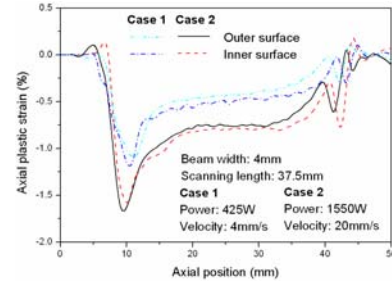


Fig. 11 Distribution of axial plastic strain along the intrados at different velocity under Scheme III

### Line-Source Axial Scanning with Water Cooling

Effect of Water Cooling on Deformation of Tube Fig. 12 compares the temperature distribution on the irradiated surface when the tube is irradiated by a continuous line-source with and without cooling giving all other processing parameters the same. It is obvious that the range of heat affected zone especially behind the laser beam can be controlled effectively by the quick removal of heat in Scheme IV. Fig. 13 shows that the time history of axial plastic strain at the centre of intrados under Scheme III and IV, respectively. The compressive axial plastic strain obtained with water cooling is much larger than that of without cooling, which shows that water cooling is helpful to increase the constraint to the heat affected zone especially in the region right behind the current location of the laser beam. Another interesting phenomenon is that the axial plastic strain at the outer and inner surfaces is both compressive and it is indicative that the upsetting mechanisms are more dominant under Schemes III and IV.

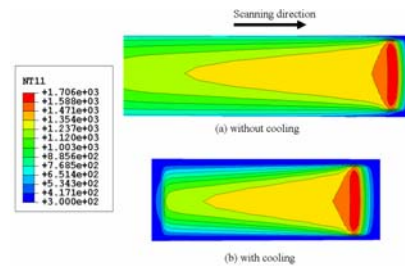


Fig. 12 Comparison of temperature distributions under the line-source axial scanning w/ and w/o cooling schemes (laser power: 1550W, scanning velocity: 20mm/s, beam width: 4mm, cooling offset: 50mm)

Relationship between Bending Radius and Cooling Offset It is known that the constraint in the axial direction plays a more important role in laser tube bending. Whether water cooling positively affects the constraint in the axial direction or not is dependent on the cooling offset (defined in Fig. 1b). The effects of

cooling offset on bending radius under two sets of processing parameters are presented in Fig. 14. The variation tendency of bending radius with the cooling offset is similar in two cases. The heat dissipates much faster with water cooling than without cooling. However, if the heated material is cooled too early by the sprinkler with a short offset ( $I=30\text{mm}$ ), it doesn't have enough time to obtain the maximal constraint from the cold surrounding material. The sprinkler with a longer cooling offset can assist in the augment of plastic strain in two aspects: one is to increase the temperature gradient between heated and cold material; the other is to keep the longer heated length which is necessary to produce large deformation. Too long an offset will lead to failure of the water sprinkler in the generation of more axial mechanical constraint.

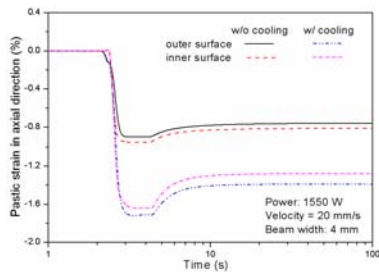


Fig. 13 Comparison of the history of axial plastic strain at the centre of intrados under Scheme III and IV

It is also seen in Fig. 14 that the optimal cooling offset at the lower velocity is smaller than that at the higher velocity. The reason is obvious that the heat affected zone is shorter due to the high heat dissipation at the lower velocity. It is seen that the bending radius with cooling at the low velocity is reduced much more than that at the high velocity. Thus, it is proven again that the low velocity without cooling is unsuitable for continuous line-source scanning as a result of higher heat dissipation and reduced mechanical constraint in the axial direction.

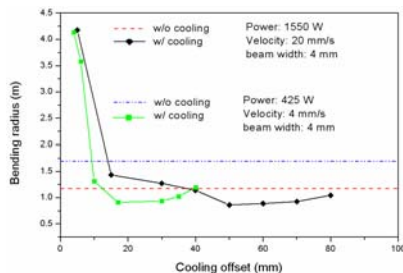


Fig. 14 Variation of bending radius with cooling offset

Under Scheme IV, simulation of a tube of 600 mm long is carried out as shown in Fig. 15a. Preliminary experiments are carried out for tubes of 1,800 mm long

with the same diameter and wall thickness (Fig. 15b). The simulation investigation reported in this paper lays groundwork for further experiments.

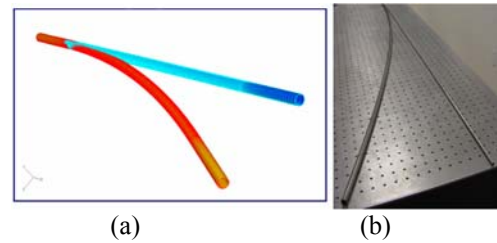


Fig. 15 Experimental and simulated results under Scheme IV for tube outer diameter: 12.7 mm, wall thickness: 0.89 mm, and tube length: (a) 600mm, and (b) 1800 mm

### Comparison of Scanning Schemes

To eliminate the effect of tube length on deformation, tubes of 100 mm in length is simulated in the following comparison of four scanning schemes. Under Scheme I, eight scans are sequentially applied with equal spacing in the axial direction. With the beam spot size equal to 11 mm, there are no significantly overlapped heating areas and yet the scans cover almost the entire tube length. Under Scheme II, twenty pulses are sequentially applied with equal spacing in the axial direction. Here the beam width in the axial direction is 4 mm and again the pulses cover almost the entire tube length without significantly overlapped heating areas.

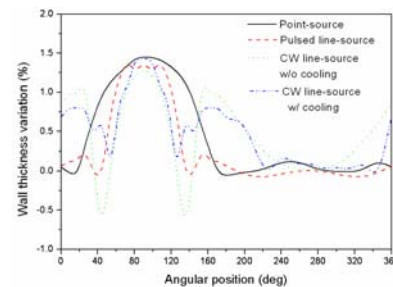


Fig. 16 Wall thickness variations under four scanning schemes

**Wall Thickness Variation** The wall thickness variation along the circumference of tube that is bent under the optimal processing conditions for each scheme listed in Table 3 is shown in Fig. 16. Under Scheme I and II, wall thickening occurs in the entire scanned range and wall thickness varies little in the unscanned range. No wall thinning at the extrados is very beneficial to bending tubes with a small bending radius and to choosing tubes with thinner wall thickness to start with. The patterns of wall thickness variation under Scheme III and IV are similar. Wall thickening is

observed mainly at the scanned range and at the edge of unscanned range as well, but the former is larger than the latter. This is due to the more prominent constraint in the circumferential direction under the Schemes. Under Scheme IV, the wall thickening fluctuates more due to more dramatic transitions from cooled and un-cooled regions.

**Cross-section Distortion** Fig. 17 shows that the cross-section of tube before and after laser bending under the same processing conditions for each scanning scheme as listed in Table 3. The cross-section distortion is quantitatively described by ovality which is defined as  $(D_{max} - D_{min})/D$ , where  $D_{max}$  and  $D_{min}$  are the maximum and minimum deformed outside diameters, respectively, and  $D$  is the outside diameter prior to deformation.

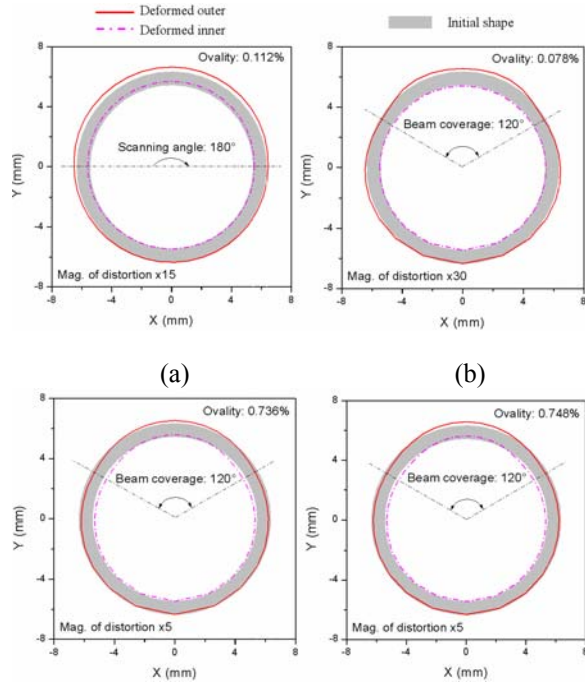


Fig. 17 Cross-section distortions (a. Scheme I; b. Scheme II; c. Scheme III; d. Scheme IV)

Under all schemes, the tube bulges out a bit in the heated area due to the tensile circumferential strain (e.g., Fig. 7) caused by the compressive axial strain. Under the three schemes using a line laser source, the boundary between heated and unheated material (i.e., at both ends of the 120-degree beam coverage) bulges in a bit primarily due to the sudden change at the boundary. Under Scheme III and IV, the cross-section distortion (0.736% and 0.748% in ovality, respectively) is larger than that under other two schemes (0.112% and 0.078% in ovality, respectively).

This is primarily because the former represents a cumulative effect of the entire axial scan, while the latter mainly accounts for the effect of a single circumferential scan (as under Scheme I) and a single pulse irradiation (as under Scheme II) as subsequent scans or pulses are regarded as independent with each other.

**Processing Efficiency** The processing efficiency under four scanning schemes is compared in Table 3. The specific energy is defined as the energy consumed to produce unit degree of bending angle. Clearly, Scheme IV fares the best from the viewpoint of energy saving. Under Scheme I and II, it is necessary to wait for the tube temperature to cool down to near the room temperature between two consecutive scans. Under Scheme III and IV, the processing time only includes the actual scanning time. It is clear that the continuous line-source axial scanning is advantageous to continuous point-source circumferential scanning in both energy consumption and processing time.

Table 3 Comparison of Four Scanning Schemes

Scheme	I	II	III	IV
Bending Angle (deg)	1.73	2.22	4.16	5.83
Bending Radius (m)	3.3	2.58	1.2	0.86
Energy Input (J)	12480	8500	6781	6781
Specific Energy (J/Deg)	7213.8	3828.8	1630	1163
Number of scanning	8	20 (pulses)	1	1
Time (sec)	Scanning	16	20	4.375
	Waiting	2100	2261	0
Tube length=100mm; Scheme I: (P=780W, W=1.58rad/s, d=1mm, 8 equally-spaced sequential circumferential scans); Scheme II: (P=425W, t=1s, w=4mm, 20 equally-spaced sequential pulses,); Scheme III: (P=1550W, v=20mm/s, w=4mm); and Scheme IV: (P=1550W, v=20mm/s, w=4mm). These conditions are optimal ones determined for each case.				

The simulations and experiments show that, although the line-source axial scanning scheme is shown to be most efficient, it appears to be difficult to generate a bending radius smaller than half a meter per scan under the process condition investigated. On the other hand, smaller bending radius can be achieved with multi-scans densely located at different axial positions under the point-source circumferential scanning scheme at the cost of heavier time and energy consumption.

## Conclusions

Four scanning schemes, namely continuous point-source circumferential scanning, pulsed line-source axial procession, continuous line-source axial scanning

without or with water cooling are investigated by numerical simulation. The numerical model is validated using existing experimental results under the first scanning scheme. Pulsed line-source axial procession can induce deformation in the tube depending on the appropriate beam coverage. In line-source axial scanning, within a certain velocity range, higher velocity can produce larger deformation due to the smaller heat dissipation and the steeper temperature gradient between the cold and heated material. The application of water cooling is helpful to increase the bending deformation. The optimal cooling offset is related to the scanning velocity. The ovality which describes the cross-section distortion in axial scanning is larger than that in circumferential scanning. The wall thickness variation is more intensive in axial scanning than that in point-source circumferential scanning. Based on the numerical analysis, it is concluded that upsetting mechanism dominates in these three axial scanning schemes. Line-source axial scanning without or with cooling is better than point-source circumferential scanning in processing efficiency.

### Acknowledgement

The authors acknowledge the financial support from NIST under grant number ATP-00005269.

### References

- [1] Silve, S., Steen, W. M. & Podschies, B. (1998) Laser forming tubes: a discussion of principles, in Proceedings of ICALEO: Orlando, USA, Section E, 151-160.
- [2] Kraus, J. (1997) Basic process in laser bending of extrusion using the upsetting mechanism, in Proceedings of the LANE'97: Meisenbach Bamberg, Germany, Vol. 2, 431-438.
- [3] Li, W. & Yao, Y. L. (2001) Laser bending of tubes: mechanism, analysis and prediction, ASME J. Manuf. Sci. Eng., **123**, 674-681.
- [4] Bachmann, Friedrich (2002) Present technology, industrial applications and future prospects of high power diode lasers, in Proceedings of SPIE, Dan C. Dumitras, Maria Dinescu, USA, Vol. 4762, 1-5.
- [5] Lawrence, J. (2002) A comparative investigation of the efficacy of CO<sub>2</sub> and high-power diode lasers for the forming of EN3 mild steel sheets, Proc Instn Mech Engrs, Vol. 216, Part B: J Engineering Manufacture, 1481-1491.
- [6] Lopez, D., Dubslaff, J., Hofling, R. & Aswendt P. (2003) Application of a high-power diode laser for laser Bending, PIE, Vol. 3097, 692-697.
- [7] Shealy, L. David (2002) Historical perspective of laser beam shaping, in Proceedings of SPIE, Dan C. Dumitras, Maria Dinescu, USA, Vol. 4770, 28-47.
- [8] Mucha, Z., Cabaj, M., Gradon, R., Pawlowski, M. & Widlaszewski (2001) Laser forming of plates by use of beam with circular and rectangular cross section, in Proceedings of the LANE'2001, Meisenbach Bamberg, Germany, Vol. 1, 527-536.
- [9] Triantafyllidis, D., Li, L. & Stott, F.H. (2002) The effect of beam shape in laser surface treatment of ceramics, in Proceedings of ICALEO, Arizona, USA, Section E, pp.171-180.
- [10] Churchill, S.W. & Berstein, M. (1997) A correlating equation for forced convection from gases and liquids to a circular cylinder in crossflow, J. Heat Transfer, Vol. 99, 300-306.
- [11] Myers, R.H. & Montgomery, D.C. (1995) Response Surface Methodology, John Wiley & Son, 700pp.
- [12] Li, W. & Yao, Y. L. (2001) Laser forming with constant line energy, Int J Adv Manuf Technol, **17**, 196-203.

### Meet the Authors

**Jie Zhang** is a Ph.D candidate in the Department of Mechanical Engineering at Columbia University. She received a BS in 1993 and a MS in 1997 in Mechanical Engineering from Xi'an Jiaotong University, China.

**Peng Cheng** is a Ph.D candidate in the Department of Mechanical Engineering at Columbia University. He received a BS in 1997 and a MS in 2000 in Mechanical Engineering from Tsinghua University, China.

**Wenwu Zhang** is a Research Engineer at GE Global Research Center. He received a Ph.D. from Columbia University in 2001.

**Michael Graham** is a computer scientist at GE Global Research Center with a Masters degree. His area is in CAD tool development, deformation modeling, neural networks, and genetic algorithms.

**Jerry Jones** is Chief Scientist at N.A. Tech. He has a Ph.D. in Metallurgical Engineering from Colorado School of Mines. His area includes process planning and optimization, and model based simulation system for thermal forming and other processes.

**Marshall G. Jones** is a Program/Technical Manager at GE Global Research Center responsible for many laser related developments there. He has a Ph.D. in Mechanical Engineering. He is a member of NAE and a past LIA board member.

**Y. Lawrence Yao** is a Professor in the Department of Mechanical Engineering at Columbia University. He received his Ph.D. from the University of Wisconsin-Madison in 1988. He serves on the Board of Directors of LIA.